Design of Surface-mounted Permanent Magnet Synchronous Motor using Electromagnetic and Thermal Analysis

**Soo-Hwan Park[1,2], Jin-Cheol Park[1], Jun-Woo Chin[1], Hyeon-Jin Park[1],
Soon-O Kwon[2], Sung-Il Kim[3], and Myung-Seop Lim[1]***

[1]*Department of Automotive Engineering, Hanyang University, Seoul 04763, Korea*
[2]*Mechatronics Convergence Technology Group, Korea Institute of Industrial Technology, Daegu 42994, Korea*
[3]*Department of Electrical Engineering, Hoseo University, Asan 31499, Korea*

This paper proposes a design method of the surface-mounted permanent magnet synchronous motor using electromagnetic and thermal analysis. Since the electromagnetic and thermal fields are related, the permanent magnet synchronous motor should be considered not only in terms of the power density but also the thermal characteristics. The analytic method was used to investigate the power density of the concentrated winding model using the same number of poles. In the thermal design process, the analytic prediction was carried out by using the electromagnetic and thermal analysis called the lumped parameter thermal network (LPTN). The optimized geometry and losses which were calculated by the electromagnetic finite-element analysis were considered in the LPTN. As a result, an improved model was designed with superior power density and thermal characteristics to the prototype. Finally, the experiments were conducted to verify the validity of the design process and results.

Keywords : electromagnetic and thermal analysis, lumped parameter thermal network, pole and slot combination, surface-mounted permanent magnet synchronous motor

1. Introduction

Permanent magnet synchronous motor (PMSM) have used in all applications requiring motion control, because of its high power density and low maintenance cost. One of the main goals of the PMSM design is to produce a high power density machine with low heat generation [1, 2]. This paper deals with the design methodology of the surface-mounted permanent magnet synchronous motor (SPMSM) using electromagnetic-thermal analysis. As a result of the design, the power density and thermal characteristics of the improved model were improved.

The power density, the electromagnetic performance of the PMSM, is determined by the circuit parameters such as the resistance, inductance, and back-electromotive force (Back-EMF), which are the factors of voltage drop. To improve the power density, it is advantageous to have low resistive and inductive voltage drop which are the

factors of decreasing the output power. However, the circuit parameters are influenced by various factors such as the magnetic circuit, the number of turns and the diameter of the coils. Among the factors the pole and slot combination has the greatest influence on the circuit parameters. Therefore, many researchers focused on the pole and slot combination when designing the PMSM with high torque density.

Several studies discussed the torque density which is related to the winding factor that is determined by the pole and slot combinations [3-6]. These studies selected the pole and slot combination based on the high winding factor for minimizing the phase current. Moreover, the pole and slot combination has a large effect on the cogging torque [7-9]. The applications that require smooth movement have to select the pole and slot combination considering cogging torque. However, previous studies did not deal with the power density according to the change in circuit parameters as the pole and slot combination changes.

Since the magnetic field and the thermal field are related, the thermal characteristics affect the electromagnetic

*Corresponding author: Tel: +82-2-2220-4466
Fax: +82-2-2220-4467, e-mail: limmang87@hanyang.ac.kr

performance of the motor. For example, the dissipated heat causes the demagnetization of the permanent magnet and the rise of the resistance [10]. In order to predict the transient operation of the motor, thermal characteristics as well as the electromagnetic characteristics must be considered. In the thermal design process, there are two ways of predicting the thermal performance. The first method is the numerical methods such as a computational fluid dynamics (CFD). Since the CFD reflects the various boundary conditions, the complex heat flow phenomena can be analyzed accurately [11-14]. However, it takes a lot of time for the setup of the model and computation of the transient analysis [2, 12]. The second method is an analytic approach called the lumped parameter thermal network (LPTN) based on the geometry, material properties and the losses of the model [1, 15-18]. In this way, the heat sources obtained by using the electromagnetic finite element analysis (FEA) can be placed at appropriate locations on the network based on the heat transfer mechanism to predict the temperature change of the desired node.

This paper is organized as follows. In section 2, the requirements which are the goal of the improved model and the information of the prototype were described. In section 3, the LPTN and the components that construct the LPTN were explained. The thermal resistance and the heat transfer coefficients that make up the LPTN were described in this section. Then, the stator design process to obtain high power density and better thermal characteristics was described in section 4. The design results and experiment results were described in section 5. Finally, the conclusion was drawn in section 6.

2. Analysis of Prototype

The prototype is an 8-pole and 6-slot (8P6S) SPMSM with a fractional slot double layer concentrated windings. A polar anistropic magnetized Nd-Fe-B bonded magnet of 8 poles is used for the rotor. The rated power is 55.1 W at the rated speed of 2980 rpm, rated torque of 176.6 mNm, and the rated current of 3.24 A_{rms}. When designing the improved model, the Back-EMF must be kept the same as the prototype in order to maintain the current while using the same rotor.

To analyze the thermal characteristics on the rated power of the prototype, a temperature saturation test was conducted. In order to measure the temperature trend of the end-coil, the operating time was set to 1 hour. As a result of the test, the temperature exceeded the limit temperature of 80 °C when the initial temperature is 30 °C, so it is necessary to lower the saturation temperature
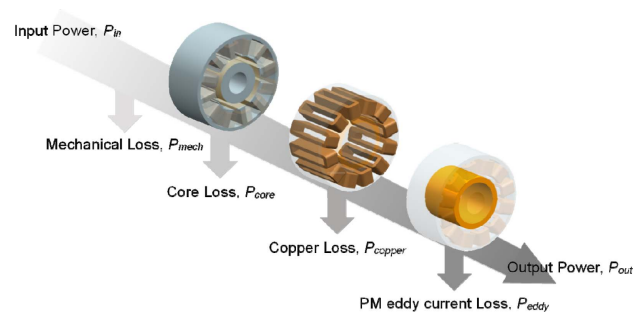

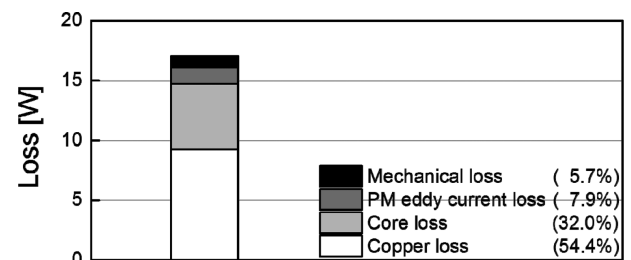Fig. 1. (Color online) Motoring loss of the PMSM.

Fig. 2. Proportions of the losses on the rated power of the prototype.

by improving the thermal characteristics.

It is important to analyze the losses because they determine the thermal characteristics of the motor. The losses of the prototype are shown in Fig. 1. The losses of the prototype consist of the electromagnetic losses and the mechanical loss. The electromagnetic losses consist of the core loss (P_{core}), the copper loss (P_{copper}), and the PM eddy current loss (P_{eddy}). The mechanical loss (P_{mech}) that dependents on the rotor speed is generated by the friction in the bearing and the airgap. The proportion of each loss is obtained from a no-load and load test on the rated power. From the no-load test, the P_{core} can be separated from the no-load loss to obtain the P_{mech} at the rated speed. The P_{copper} can be obtained from the resistance and the current from the load test, and the P_{core} and P_{eddy} can be obtained from the FEA results. The proportions of each loss are shown in Fig. 2. In this paper, the thermal characteristics were improved by reducing the P_{copper} and P_{core}, which account for 86.4 % of the entire losses.

3. Lumped Parameter Thermal Network

3.1. Background

The LPTN of SPMSM consists of the electromagnetic and thermal system. Both systems are represented by the losses and thermal lumped circuit parameters, respectively, which can be used to predict heat transfer results of the motor. To understand the thermal system, it is necessary to examine the thermal system based on the equivalence

Table 1. Equivalence between electrical and thermal system.

Name	Electrical System	Thermal System
Potential	Voltage, V	Temperature difference, ΔT
Flow	Current, I	Heat flow rate, Q
Resistance	Electrical resistance, R	Thermal resistance, R_t
Capacitance	Electrical capacitance, C	Thermal capacitance, C_t
Equation	$V = IR$	$\Delta T = QR_t$

of the two systems. As can be seen in Table 1, the voltage, which is the potential difference in electrical system, is expressed as the difference in temperature in the thermal system. In addition, the current is expressed as a heat flow rate, the electrical resistance as a thermal resistance, and the electrical capacitance as a thermal capacitance. Based on the two systems, the LPTN is constructed considering the following assumptions [15, 16].

1) The thermal radiation is ignored.

2) Except for the flow between the stator tooth and coil, there is no flow in the circumferential direction.

3) The mean temperature of the components ignoring temperature variation in the radial and axial directions.

4) The thermal capacitance and heat source are uniformly distributed in each component.

5) Natural cooling conditions without heat sink or water jacket.

3.2. Thermal resistance

In the conduction, the heat flow is within and through the body itself. The conduction occurs inside each part of the motor such as the yoke and tooth of the stator, the rotor, the PM, and the housing. Since the shape of the aforementioned component is the same in the axial direction, it can be simplified as shown in Fig. 3(a). Each component consists of four thermal resistances as stated in Eq. (1)-(4) [1].

$$R_{t,L} = \frac{L_{stk}}{6\pi k_L (r_1^2 - r_2^2)} \tag{1}$$
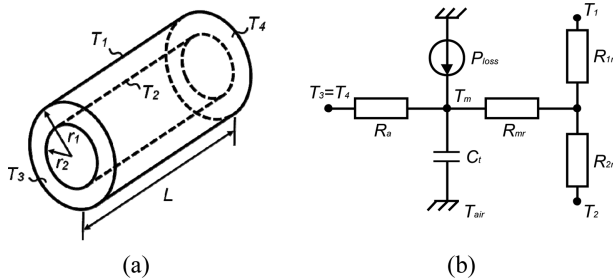

(a)   (b)

Fig. 3. Element of conduction heat transfer. (a) A simplified shape of the component and (b) thermal network of the thermal resistance.

$$R_{t,1r} = \frac{1}{2\pi k_r L_{stk}} \left[1 - 2r_2^2 \ln\left(\frac{r_1}{r_2}\right) \Big/ (r_1^2 - r_2^2) \right] \tag{2}$$

$$R_{t,2r} = \frac{1}{2\pi k_r L_{stk}} \left[2r_1^2 \ln\left(\frac{r_1}{r_2}\right) \Big/ (r_1^2 - r_2^2) - 1 \right] \tag{3}$$

$$R_{t,mr} = \frac{\left[r_1^2 + r_2^2 - 4r_1^2 r_2^2 \ln\left(\frac{r_1}{r_2}\right) \Big/ (r_1^2 - r_2^2) - 1 \right]}{4\pi (r_1^2 - r_2^2) k_r L_{stk}} \tag{4}$$

where $R_{t,L}$ is an axial direction thermal resistance, $R_{t,1r}$, $R_{t,2r}$, represent the outward and inward radial direction thermal resistance, and $R_{t,mr}$ is the compensation resistance. L_{stk} is the stack length of the core, r_1 and r_2 are the outer and the inner radius of the simplified shape in Fig. 3(a), respectively, k_L is the axial thermal conductivity, and k_r is the radial thermal conductivity. These resistances are modeled as a conduction thermal network as shown in Fig. 3(b) to represent a single component of the motor. The losses of each component are modeled as a heat source to form the network.

Convection is caused by the movement of the fluid like air in the airgap. Therefore, the convection of the motor is affected not only by the physical dimension of each component but also by the condition of the fluid.

In this paper, the convections which occur in the airgap, ambient, and the air between the end cover and motor are considered. The convection thermal resistance, R_{conv}, is expressed in Eq. (5).

$$R_{conv} = \frac{1}{hA} \tag{5}$$

where h is the convective heat transfer coefficient, and A is the area where the convection occurs. h is determined by the *Reynolds* number, *Nusselt* number, and the *Prantl* number which represent the condition of the fluid [18].

3.3 Heat source and thermal capacitance

The heat source in the motor is equal to the losses of Fig. 1. The losses are expressed as the current source in the network. For the accuracy of the thermal analysis, each loss is calculated separately for each component to reflect the exact location. P_{copper} is split into the coil-side and end coil, and P_{core} is divided into components of the yoke, tooth, tooth tip and the rotor as shown in Eq. (6)-(7).

$$P_{copper} = P_{coil-side} + P_{end-coil} = 3I_a^2 R_a \tag{6}$$

$$P_{core} = P_{yoke} + P_{tooth} + P_{tooth-tip} + P_{rotor} \tag{7}$$

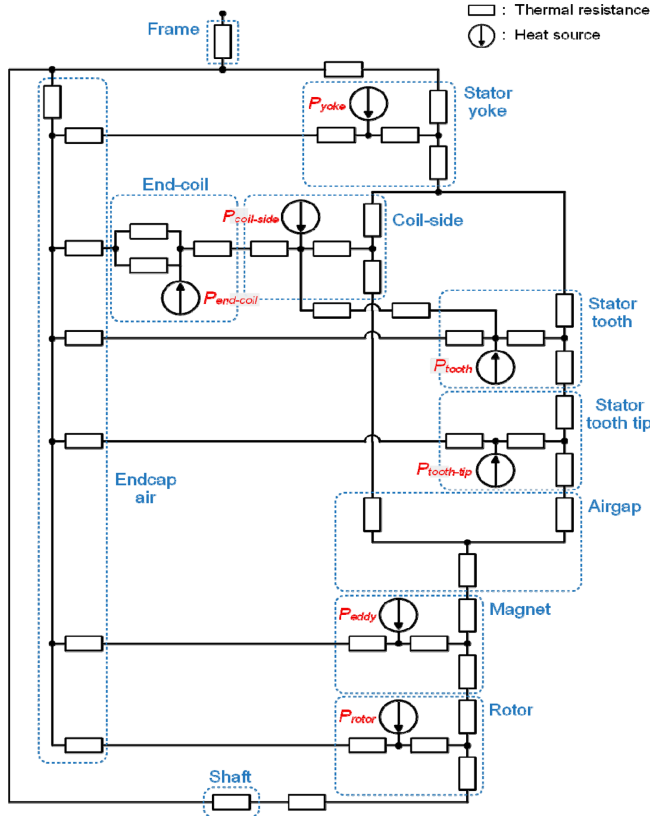where the P_{copper} is the copper loss that is proportional to

Fig. 4. (Color online) Lumped parameter thermal network for the SPMSM.

the magnitude of the resistance, R_a, and the phase current in rms, I_a.

The P_{core} based on the core material is divided into hysteresis loss, eddy current loss, and the abnormal loss as stated in [19]. Since each loss varies with the frequency and the magnetic flux density, it is calculated by the electromagnetic FEA.

According to the method to calculate the P_{core} described in [20], the magnetic flux density of each node is separated into frequency dependent harmonic components for one electrical period after the FEA. After that, the core loss according to the frequency and the flux density is calculated from the core loss data of the material, and the core

loss of the whole element is summed to calculate the total P_{core}. The P_{eddy} is calculated by 3-D FEA because it is necessary to consider the induced voltage by magnetic flux variation in axial direction at PM.

The thermal capacitance, which is the amount of the thermal energy required to raise the temperature of the object, is related to the volume of the object. The thermal capacitance, C_t, is calculated with the dimensions, the mass density, ρ, and the specific heat, c_p of the material as shown in

$$C_t = \rho c_p \pi (r_1^2 - r_2^2) L_{stk} \qquad (8)$$

From the conduction and convection components of the LPTN, the LPTN is modeled as Fig. 4. In addition, the thermal contact resistances are considered. $R_{t,frame}$ is the thermal contact resistance between the frame and the stator, and the $R_{t,shaft}$ represents the thermal contact resistance between the shaft and the rotor. $R_{t,slot-liner}$ and $R_{t,coil-tooth}$ are the thermal resistance of the slot liner and the thermal resistance between the coil and the stator tooth, respectively.

4. Improved Design

4.1. Pole and slot combination

When selecting the pole and slot combination, the winding factor, the distribution of the radial electromagnetic force, and the least common multiple (LCM) of the pole and slot combination should be considered. The candidates of the pole and slot combinations for improved model are the 8-pole and 6-slot (8P6S), 8-pole and 9-slot (8P9S), and 8-pole and 12-slot (8P12S). The Back-EMF, e_a, which is related to the torque is given by

$$e_a = \omega_m p k_{w1} N_{ph} \Phi_{m1} \qquad (9)$$

where ω_m is the speed of the rotor, p is the number of pole pairs, k_{w1} is the winding factor of the fundamental components, N_{ph} is the series turns per phase, Φ_{m1} is the airgap flux per pole due to the magnet. If N_{ph} is the same, the Back-EMF is proportional to the winding factor.

The period of the cogging torque is equal to the LCM of the number of pole pairs and slots, s, as shown in Eq. (10).

$$n = LCM(s, 2p) \qquad (10)$$

8P9S has the best electrical performance as it has the highest winding factor and the LCM. However, according to the study of [21, 22], 8P9S is excluded from the candidates because it has an asymmetric force distribution that is vulnerable to noise and vibration.

8P6S and 8P12S generate the same torque when the current is the same because the winding factors are the same. However, the resistance and the inductance, which are the important factors that determine the P_{copper} and the output power, are different. When the number of poles and other conditions such as the diameter of the coil, N_{ph} are the same, the resistance and the inductance are proportional to the slot pitch.

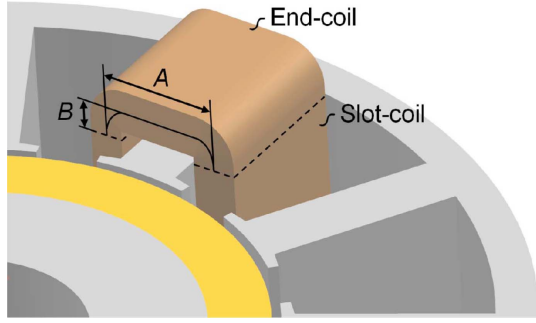The resistance which is affected by the length difference of the end turns is shown in

Fig. 5. (Color online) Averaged coil span and assumed height of the end-coil.

$$R_a = \rho_c \frac{4}{\pi} \frac{2(L_{stk} + l_{end})N_{ph}}{d^2}\left[1 + \alpha(T - 20°C)\right] \qquad (11)$$

where

$$l_{end} = A + 2B \qquad (12)$$

where ρ_c is the resistivity of copper at 20°C, l_{end} and d are the length of the end-coil and the diameter of the coil, A and B are the average coil span and the assumed average height of the end-coil, respectively, as shown in Fig. 5. T and α are the operating temperature and the temperature coefficient of the resistivity, respectively. Since the resistance of 8P12S which related to the coil span is smaller than that of 8P6S, the P_{copper} of 8P12S is smaller than those of 8P6S as shown in Eq. (6), (11).

The inductance is important because the inductive voltage drop absorbs a fraction of the supply voltage, tending to limit the maximum speed that can be attained with any given torque. The dynamic model of the SPMSM in BLDC control can be derived from the voltage equation of the electric motor. The voltage equation in frequency-domain is expressed as

$$V_a = (R_a + jp\omega_e L_a)I_a + E_a$$
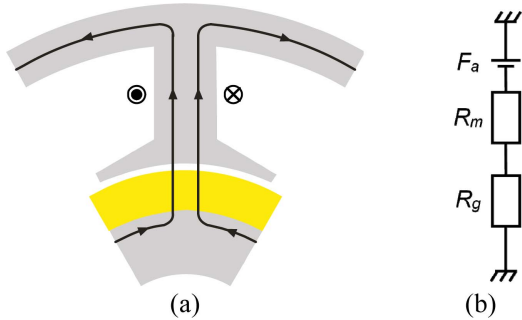$$= (R_a + jp\omega_e L_a)\frac{T_L}{k_t} + k_e \omega_m \qquad (13)$$

Fig. 6. (Color online) Flux lines with (a) a single phase current only and (b) equivalent magnetic circuit.

where V_a, I_a, and E_a are the armature voltage, current, and the Back-EMF per phase in frequency-domain, respectively, T_L and p is the torque and the number of pole pairs, R_a, L_a, k_e, and k_t are the resistance, inductance per phase, the Back-EMF constant and the torque constant, respectively. From the equation (13), then maximum speed, $\omega_{m,max}$, in any given torque, T_L, is derived as Eq. (14).

$$\omega_{m,max} = \frac{V_a k_t - R_a T_L}{jpL_a T_L + k_e k_t} \qquad (14)$$

According to Eq. (14), it is advantageous to improve the output power by choosing the pole and slot combination with the small inductance. To calculate the inductance, a magnetic circuit per single coil can be simplified as shown in Fig. 6(a) and Fig. 6(b). In the simplified model, the relative permeability of the core is assumed to be infinite and the magnetic flux path in the airgap is assumed to be perpendicular to the magnet surface. The inductance per phase is equal to the sum of the self and the mutual inductance as shown in Eq. (15), when the end-turn and the slot-leakage inductance are ignored.

$$L_a = \frac{s}{m}(L_s - L_m) \qquad (15)$$

As the magnetic flux of 8P6S and 8P12S is divided half by the neighboring teeth, mutual inductance is half of the self-inductance. The self and mutual inductance are related to the magnetic resistance and the number of series turns as shown in Eq. (16)-(17).

$$L_s = \left(\frac{N_{ph}}{s/m}\right)^2 \frac{1}{2(R_{m,g} + R_{m,PM})}, \quad L_m = -\frac{L_s}{2} \qquad (16)$$

$$R_{m,g} = \frac{sl_g}{\mu_0 \pi DL_{stk}}, \quad R_{m,PM} = \frac{sl_{PM}}{\mu_0 \pi DL_{stk}} \qquad (17)$$

where L_a is the inductance per phase, L_s and L_m are the self and mutual inductance per one coil, N_{ph} is the series turns per phase, s and m are the number of slots and phase, $R_{m,g}$ and $R_{m,PM}$ are the reluctance of the airgap and the PM, l_g and l_{PM} are the length of the airgap and the PM, D and L_{stk} are the diameter of the mean airgap diameter and the stack length of the core, respectively. The phase inductance is calculated by the series and parallel structure of the electric circuit and the inductance of each single coil. The magnetic circuit due to the armature current in a single coil is determined by the reluctances of the airgap and permanent magnets as shown in Fig. 6(b). Since the cross-sectional area of the airgap and permanent magnet are determined by the slot pitch, the slot pitch is the main variable for calculating the inductance. The number of turns per each single coil and
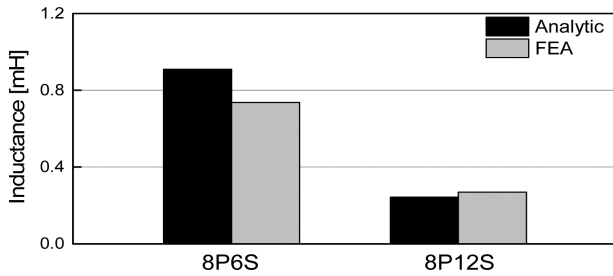
Fig. 7. Comparison of the phase inductance between 8P6S and 8P12S.

Fig. 8. Electromagnetic and thermal design process of the stator of SPMSM.

cross-sectional area of the airgap and permanent magnet of 8P12S are smaller than that of the 8P6S, because the number of slots of 8P12S is twice as that of 8P6S. Thus, the inductance of single coil is eight times smaller than that of 8P6S by using Eq. (16) and (17). Consequently, the phase inductance of 8P12S is four times smaller than that of 8P6S because the series and parallel structure of the electric circuit of each model by using Eq. (15). The calculated results of the phase inductance and validation results by using the FEA are shown in Fig. 7. The frozen permeability method of [23] was used to calculate the flux linkage due to the armature current considering the magnetic saturation in the stator and rotor. The load condition is set to the rated torque in the FEA. The analytically calculated inductance of 8P12S was 0.24 mH and it was 73.6 % less than that of 8P6S. As a result, the maximum speed and the output power of 8P12S were larger than that of 8P6S at the rated torque.

According to the study of [24], the P_{eddy} of concentrated winding is affected by the pole and slot combinations. The low order spatial harmonics of the armature magneto-motive force(MMF) cause a large amount of P_{eddy}. 8P6S which is the pole and slot combination of the prototype has a lower spatial order of armature MMF than 8P12S, so the PM eddy current of the 8P6S is larger than that of the 8P12S. Considering the vibration, the cogging torque, and the electromagnetic performance as discussed above, 8P12S is suitable for the improved model.

4.2. Thermal design of the stator

The most important variables in designing the stator are the yoke and tooth width which are related to the magnetic saturation and the slot area. As the magnetic saturation occurs, the current for obtaining the same torque becomes larger. Furthermore, the copper loss and core loss can be increased. Increased losses due to the change in the reluctances acts as the heat sources and degrades the thermal characteristics. In addition, the thermal characteristics can be changed because the widths of the tooth and yoke affect to the thermal resistance. Therefore, not only the
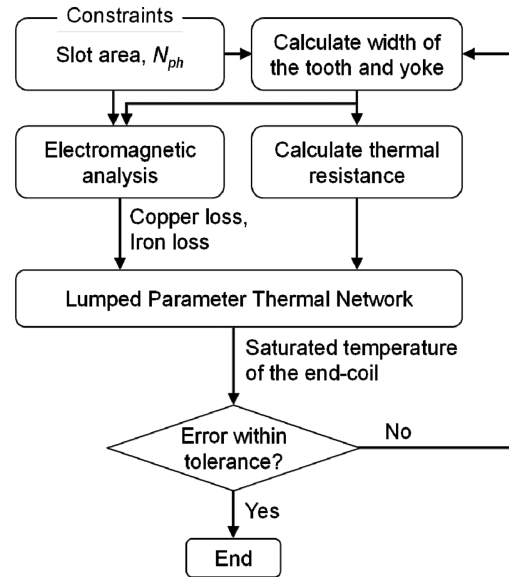
electromagnetic characteristics but also the thermal characteristics changes according to the stator design, so it is necessary to consider both characteristics.

Fig. 8 shows the design process of the stator considering the electromagnetic and thermal characteristics. First, the electromagnetic analysis was conducted according to the width of the tooth and yoke. The heat source was calculated through the electromagnetic analysis, and the thermal resistances were also calculated according to the width of the tooth and yoke. Then, the LPTN of Fig. 4 was constructed by using the heat sources and thermal resistances. In order to consider the thermal characteristics, thermal analysis using the LPTN was performed and the saturation temperature of the end-coil was calculated. Finally, the design of the stator was completed by searching for the point where the saturation temperature of the end-coil was minimized.

Before designing the stator, N_{ph} and the core material need to be determined. N_{ph} was determined as 80 turns in order to generate the same MMF as the prototype. The core material of the stator was changed from non-oriented electrical steel 50A700 to 50A470 in order to reduce the P_{core}. The P_{core} of 50A470 at 1.5 T and 200 Hz is about 34.6 % lower than 50A700. The slot area was determined by the area of the conductors in the slot and the fill factor. The diameter of the coil was increased from 0.70 mm to 0.85 mm in order to reduce the P_{copper} in the coil by decreasing the resistance. The slot area was 63.9 mm^2. Fig. 9(a)-(d) shows the normalized copper loss, core loss, thermal resistance of a single tooth and the saturation temperature of the end-coil according to the widths of the
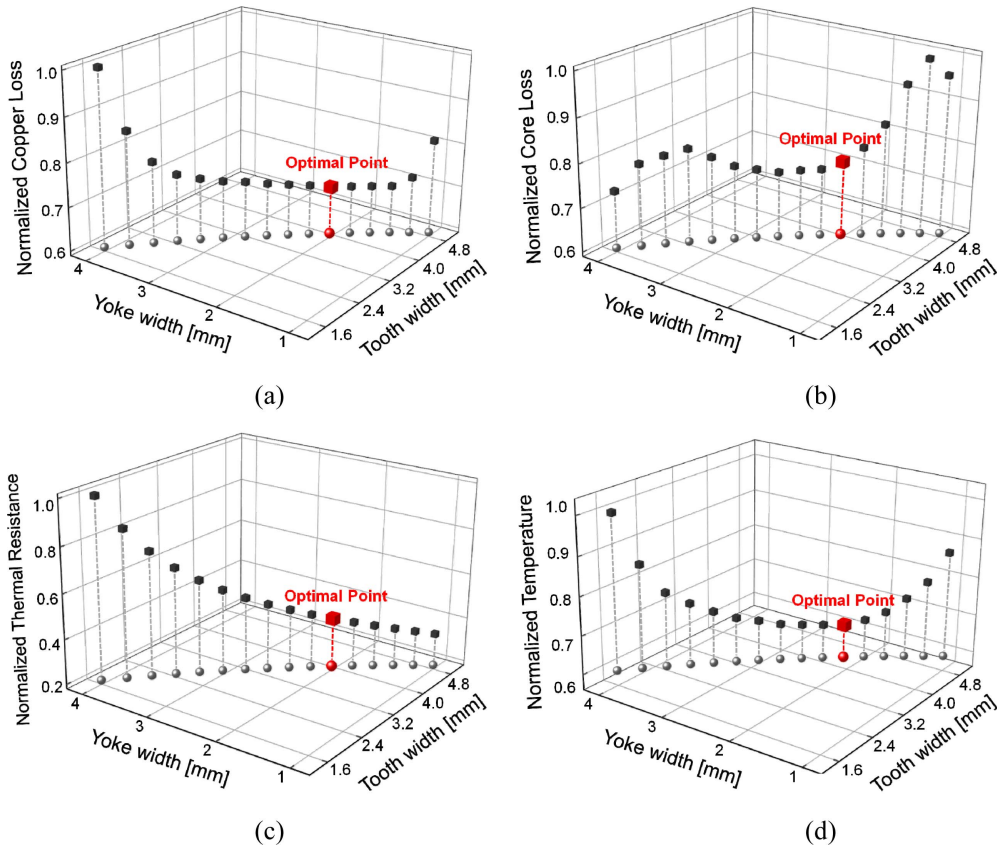
Fig. 9. (Color online) Design results of the improved model.

tooth and yoke. Since the slot area is specified as a constraint, the width of the yoke decreases as the width of the tooth increases. The yoke width of the optimum point was about half of the tooth width. Since the reluctance of the stator at optimum point was the smallest, the armature current required to generate the rated torque was the smallest, and the copper and core losses were also small in the optimum point as shown in Fig. 9(a) and Fig. 9(b). However, as the width of the tooth became smaller, the thermal resistance became larger and the heat dissipation characteristics were degraded as shown in Fig. 9(c). Nevertheless, the optimum point has a poor heat dissipation characteristics, the saturation temperature of the end-coil was lowest as shown in Fig. 9(d) because the heat sources of the optimum point were smallest.

Unlike the heat dissipation characteristics of Fig. 9(a) and Fig. 9(b), it can be seen that the end-coil temperature was minimum at the point where the heat sources were minimum. Therefore, the thermal characteristics of this model depend on the heat sources rather than the heat dissipation characteristics.

4.3. Design results

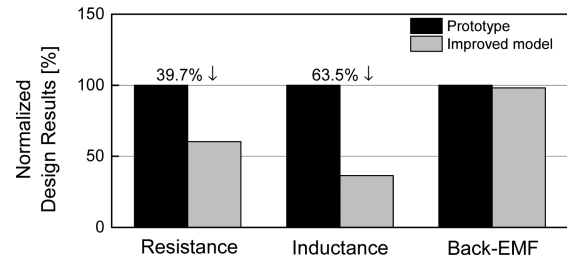Fig. 10 shows the circuit parameters of the improved

Fig. 10. Comparison of the circuit parameters between the prototype and improved model.

model compared with the prototype. As a result of changing the pole and slot combination and the diameter of the coil, the resistance and inductance were decreased by 39.7 % and 63.5 %, respectively. The loss analysis results of the improved model compared to the prototype are shown in Fig. 11. The total loss of the improved model was 9.4 W, which was reduced by 41.4 % compared to the prototype. Since the resistance of the improved model was reduced, the P_{copper} was reduced by 34.4 % compared to the prototype. The P_{core} was decreased by 42.6 %, because the stator core material changed from 50A700 to 50A470. In addition, the P_{eddy} was reduced by 84.6 %. However, the P_{mech} of the improved model was the same as the
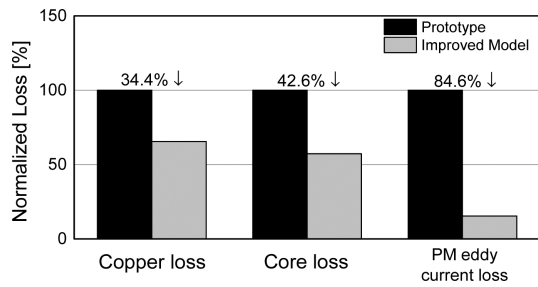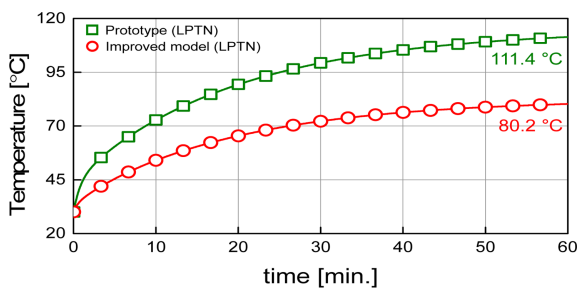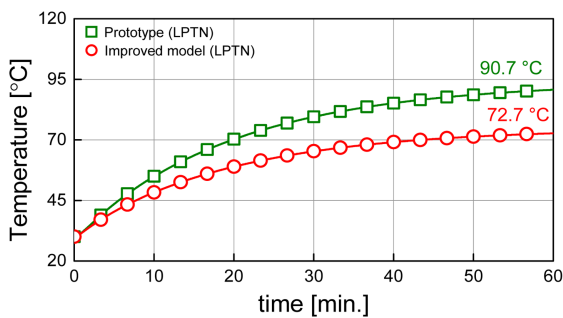
Fig. 11. Comparison of the losses between the prototype and improved model.


(a)

(b)

Fig. 12. (Color online) Simulated temperature of the (a) end-coil and (b) housing.

prototype because the same rotor was used and the speed of the rotor was the same. Based on the loss analysis results, the thermal analysis of the prototype and improved model were conducted by using the LPTN. In the analysis, the geometry and the losses of each model were considered. The analysis time was set to 60 minutes and the ambient temperature was about 30 °C. The saturation temperature of the end-coil and housing of prototype and improved model are shown in Fig. 12(a) and Fig. 12(b). The results showed that the thermal characteristics of the improved model are better than that of the prototype because of the reduced losses and the larger contact area of conductor and stator core. The predicted saturation temperature of the improved model from the simulation was 80.2 °C, which was satisfying the design requirement.
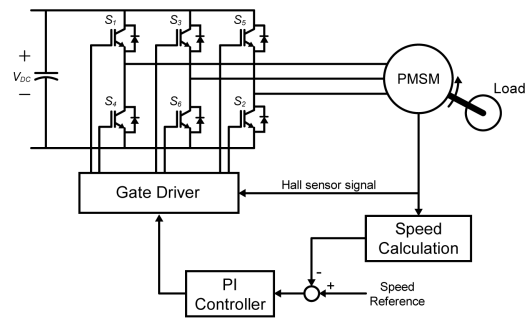
(a)
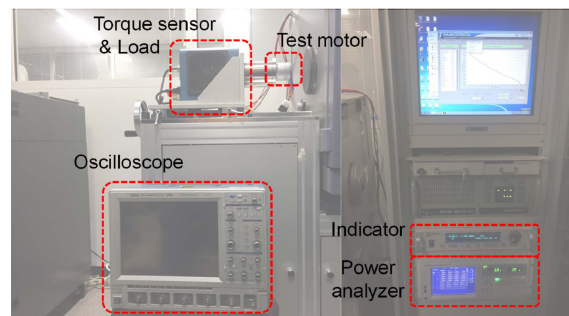
(b)

Fig. 13. (Color online) Setup of (a) the simulation and (b) test for TN-curve.

5. Experimental Verification

5.1. Comparison of the electromagnetic performance

In order to analyze the torque and speed characteristics of the prototype and the improved model, a simulation using a MATLAB Simulink was conducted. For the simulation, the motor, inverter, and the mechanical system were modeled as shown in Fig. 13(a). The electrical and mechanical parameters of the system were considered to the simulation. The setup of the test is shown in Fig. 13(b). The Magtrol TM302 torque sensor and Yokogawa WT1800 power analyzer were used in experiments to verify the simulation result. Fig. 14(a) is the simulation and test results of the two models for the torque and speed characteristics. As the resistance and the inductance of the improved model were lower than 3the prototype, the speed of the entire torque was improved. Fig. 14(b) compares the output power of the prototype and improved model. The rated power of the improved model was increased by 23.8 % compared to the prototype which satisfies the design requirement. The comparison results of the electromagnetic performance between the prototype and improved model are presented in the Table 2. As a result, the power density of the improved model was increased by 23.8 % than the prototype.
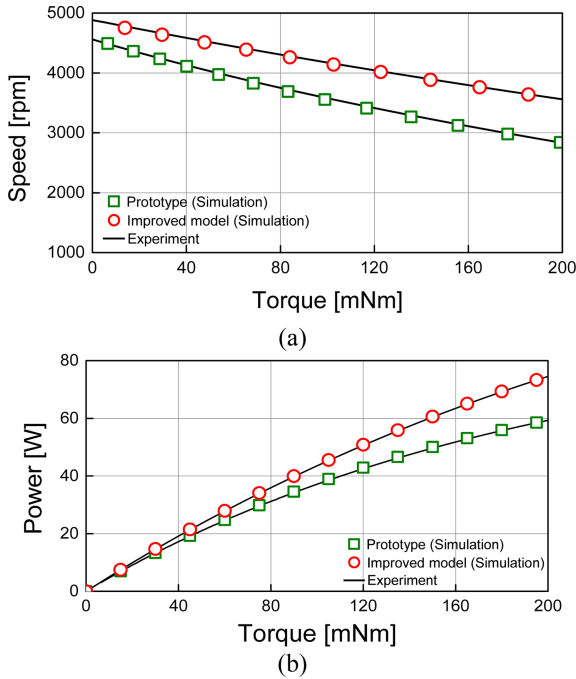
Fig. 14. (Color online) Comparison of (a) the torque and speed characteristics and (b) output power between the prototype and improved model.

Table 2. Comparison of the specifications between the prototype and improved model.

Name	Unit	Prototype	Improved model
Poles	-	8	8
Slots	-	6	12
Rated torque	mNm	176.6	176.6
Phase resistance	Ω	0.290	0.175
Phase inductance	mH	0.74	0.27
Phase Back-EMF (1,000 rpm)	V_{rms}	2.17	2.13
Rated power	W	55.1	68.2
Power density	kW/m^3	1002.5	1240.8

5.2. Comparison of the thermal characteristics

In order to verify the simulation results of the LPTN, the experiments were conducted to measure the temperature trend of the end-coil and housing. The experiments were conducted under the same conditions as the simulation. The measured temperature of the coil and housing of prototype and improved model are shown in Fig. 15(a) and Fig. 15(b). As a result of the experiments, the saturation temperature of the improved model satisfied the specification and the saturation temperature of the end-coil was lowered by 28.0 % and the housing was also lowered by 19.8 % compared to the prototype.
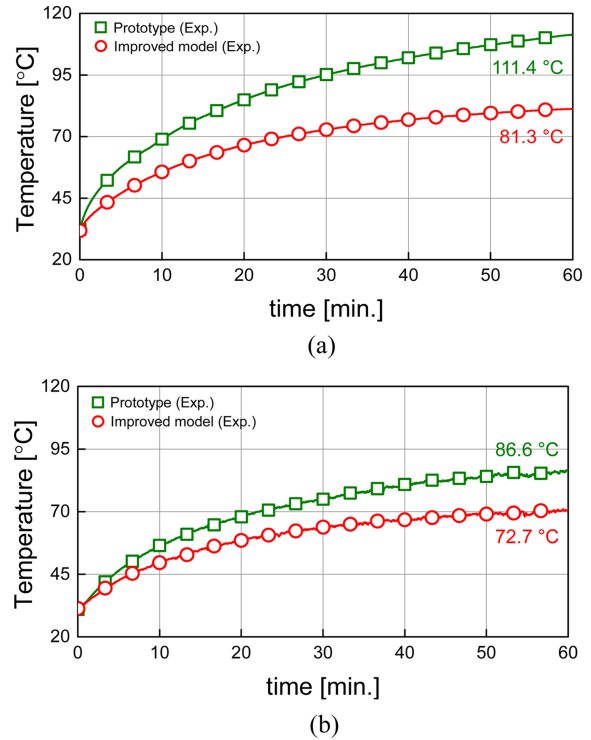

Fig. 15. (Color online) Measured temperature of the (a) end-coil and (b) housing.

6. Conclusion

In this paper, the design process for the SPMSM using the electromagnetic and thermal analysis was proposed. The LPTN was used in this paper because of the LPTN is the computationally efficient solution in thermal analysis. In order to improve the power density, a pole and slot combination with low resistive and inductive voltage drop was chosen. In addition, the thermal characteristics were improved by thermal design of the stator. In stator design process, the electromagnetic losses were reduced and the thermal characteristics were verified by the LPTN. Then, the electromagnetic performance and thermal characteristics of the prototype and improved model were compared. The compared results were verified by experiments. Consequently, the power density of the improved model was improved by 23.8 % than the prototype, and the saturation temperature of the end-coil was decreased by 28.0 % than the prototype.

Acknowledgements

References

[1] B. H. Lee, K. S. Kim, J. W. Jung, J. P. Hong, and Y. K. Kim, IEEE Trans. Magn. **48**, 2949 (2012).

[2] C. Kral, A. Haumer, M. Haigis, H. Lang, and H. Kapeller, IEEE Trans. Energy Convers. **24**, 809, (2009).

[3] R. Wrobel and P. H. Mellor, IEEE Trans. Energy Convers. **23**, 9802622 (2008).

[4] N. Bekka, M. E. H. Zain, N. Bernard, and D. Trichet, IEEE Trans. Energy Convers. **31**, 1153 (2016).

[5] K. Wang, Z. Q. Zhu, G. Ombach, M. Koch, S. Zhang, and J. Xu, IEEE Trans. Ind. Appl. **50**, 3685 (2014).

[6] G. J. Li, B. Ren, and Z. Q. Zhu, IET Electr. Power Appl. **11**, 1023 (2017).

[7] J. M. Kim, M. H. Yoon, J. P. Hong, and S. I. Kim, IET Electr. Power Appl. **10**, 691 (2016).

[8] L. Gasparin, A. Cenigoj, S. Markic, and R. Fiser, IEEE Trans. Magn. **45**, 1210 (2009).

[9] M. S. Islam, S. Mir, and T. Sebastian, IEEE Trans. Ind. Appl. **40**, 813 (2004).

[10] O. Wallscheid and J. Bocker, IEEE Trans. Energy Convers. **31**, 354 (2016).

[11] A. Nollau and D. Gerling, IEEE Int. Electric Machines and Drives Conference 456 (2013).

[12] H. Li and Y. Shen, IEEE Trans. Energy Convers. **30**, 991 (2015).

[13] Y. Huang, J. Zhu, and Y. Guo, IEEE Trans. Magn. **45**, 4680 (2009).

[14] K. Zhou, J. Pries, and H. Hofmann, IEEE Trans. Transp. Electrification **1**, 138 (2015).

[15] P. H. Mellor, D. Roberts, and D. R. Turner, IEE Proc. B Electr. Power Appl. **138**, 205 (1991).

[16] G. D. Demetriades, H. Z. de la Parra, E. Andersson, and H. Olsson, IEEE Trans. Power Electron. **25**, 463 (2010).

[17] J. Fan, C. Zhang, Z. Wang, Y. Dong, C. E. Nino, A. R. Tariq, and E. G. Strangas, IEEE Trans. Magn. **46**, 2493 (2010).

[18] D. Staton and A. Cavagnino, IEEE Trans. Ind. Electron. **55**, 3509 (2008).

[19] G. Novak, J. Kokosar, A. Nagode, and D. S. Petrovic, IEEE Trans. Magn. **51**, 2001507 (2015).

[20] M. S. Lim, S. H. Chai, J. S. Yang, and J. P. Hong, IEEE Trans. Ind. Electron. **62**, 7827 (2015).

[21] D. Y. Kim, M. R. Park, J. H. Sim, and J. P. Hong, IEEE/ASME Trans. Mechatronics **22**, 1554 (2017).

[22] T. Sun, J. M. Kim, G. H. Lee, J. P. Hong, and M. R. Choi, IEEE Trans. Magn. **47**, 1038 (2011).

[23] G. T. de Paula, J. R. B. de A. Monteiro, T. E. P. de Almeida, M. P. de Santana, and W. C. A. Pereira, 2014 IEEE 23rd int. Symposium on Industrial Electronics (2014).

[24] M. Nakano, H. Kometani, and M. Kawamura, IEEE Trans. Ind. Appl. **42**, 429 (2006).